JOURNAL OF AIRCRAFT
Vol. 42, No. 5, September–October 2005

Modeling Delta Wing Limit-Cycle Oscillations Using a High-Fidelity Structural Model

Peter J. Attar*
Computational Sciences Branch, Wright–Patterson AFB, Ohio 4533-7913
and
Earl H. Dowell† and John R. White‡
Duke University, Durham, North Carolina 27708

Flutter and limit-cycle oscillations(LCO) of a delta-wing model are studied theoretically and correlated with results from an earlier experiment and an earlier simpler theoretical model. The present theoretical model uses a high-fidelity nonlinear structural model and a linear vortex lattice aerodynamic model. The commercial finite element package ANSYS is selected to model the structure and is coupled to the vortex lattice aerodynamic model using a subiteration procedure to carry out time simulations. The delta-wing model is studied for five angles of attack (0, 1, 2, 3, and 4 deg) and for various flow speeds. Theoretical results are calculated for two different root-chord boundary conditions, that is, fully fixed and also another that allows some in-plane movement at the root chord by attaching stiff in-plane springs that connect the structure to the root boundary. The results obtained using the high-fidelity structural model are compared to earlier results computed using a lower-fidelity von Kármán plate theory. For all angles of attack studied here, the correlation between theory and experiment is better for the aeroelastic model, which uses the high-fidelity (ANSYS) structural model. Both flutter velocity and frequency as well as the LCO amplitudes and frequencies that are predicted using the higher-fidelity stuctural model correlate well with experiment. In particular the flutter and LCO results predicted using the high-fidelity structural model are similar, both qualitatively and quantitatively, for the two different in-plane boundary conditions. However the results obtained from the von Kármán model differ substantially for the two different in-plane boundary conditions.

Nomenclature

A_b	=	bound circulation aerodynamic influence coefficient matrix
A_w	=	wake circulation aerodynamic influence coefficient matrix
B	=	strain-displacement matrix
B_l	=	strain-displacement matrix in local, convected coordinate system
C	=	element damping matrix
D	=	elasticity matrix which is a function of E and G
E	=	elastic modulus
$\boldsymbol{ET}$	=	structural mesh to aerodynamic mesh interpolation matrix
$F(x, y, z, t)$	=	wing surface function
$\{\boldsymbol{F}_b\}$	=	vector of element body forces
$\boldsymbol{F}_{\text{int}}$	=	element force caused by strain
$\{\boldsymbol{F}_t\}$	=	vector of element surface tractions
$\boldsymbol{F}^P$	=	element load caused by pressure
G	=	shear modulus
$\boldsymbol{K}$	=	element stiffness matrix
$\boldsymbol{K}_{\text{consistent}}$	=	element stiffness matrix formed using consistent methodology
$\boldsymbol{M}$	=	element mass matrix
$\boldsymbol{N}$	=	shape function matrix
$\boldsymbol{N}_n$	=	normal direction shape function matrix
$\{\boldsymbol{P}\}$	=	element pressure vector
p	=	pressure
p_∞	=	freestream pressure
q	=	relative velocity between the undisturbed fluid and the wing
r	=	distance from wing to point where velocity caused by potential is being evaluated
S	=	element area
s, t	=	shell element local coordinate directions
T_l	=	element coordinate transformation matrix
t	=	time
U	=	elastic strain energy
$\boldsymbol{U}_\infty$	=	freestream flow velocity vector
u_x	=	displacement in x direction
u_y	=	displacement in y direction
u_z	=	displacement in z direction
V	=	element volume
W	=	external work
W^i	=	external work caused by inertia
W^P	=	external work caused by pressure
x, y, z	=	global coordinate system directions
α	=	angle of attack
β	=	stiffness damping coefficient
Γ_b	=	bound circulation
Γ_w	=	wake circulation
γ_{xy}	=	shear strain in xy plane
δ	=	variational operator
ε_x	=	normal strain in x direction
ε_y	=	normal strain in y direction
θ_x	=	rotational degree of freedom about x axis
θ_y	=	rotational degree of freedom about y axis
ν	=	Poisson's ratio
ρ	=	material density
ρ_∞	=	freestream flow density
σ_x	=	normal stress in x direction
σ_y	=	normal stress in y direction

Presented as Paper 2004-1692 at the AIAA/ASME/ASCE/AHS/ASC 45th Structures, Structural Dynamics, and Materials Conference, Palm Springs, CA, 19–22 April 2004; received 4 June 2004; revision received 28 July 2004; accepted for publication 29 July 2004.

*NRC Fellow, AFRL/VAAC, 2210 Elighth Street, Building 146,225; Peter.Attar@wpafb.af.mil. Member AIAA.

†William Holland Hall Professor, Department of Mechanical Engineering and Materials Science and Director of the Center for Nonlinear and Complex Systems; also Dean Emeritus, Pratt School of Engineering, Box 90300; dowell@ee.duke.edu. Honorary Fellow AIAA.

‡Research Assistant, Department of Mechanical Engineering and Materials Science; jrwhite@duke.edu.

τ_{xy} = shear stress in xy plane
Φ = velocity potential

Superscripts

i, j, k, l = element i, j, k, and l nodes
$es1, es2$ = displacement superscripts that describe element degrees of freedom

I. Introduction

FLUTTER and limit-cycle oscillations (LCO) for a delta-wing plate model have been studied recently both theoretically and experimentally by Tang et al.[1,2] and Attar et al.[3,4] In these investigations, the structural theory used was the nonlinear plate model of von Kármán. This model was solved using a normal mode expansion of the physical deflections and Lagrange's equation. This structural model was combined with a three-dimensional vortex lattice aerodynamic theory to determine the flutter and LCO characteristics of the wing in low subsonic flow. In these investigations, the correlations of the theoretical and experimental flutter and LCO results were favorable for small angles of attack and small LCO magnitudes. However as the angle of attack was increased or the flow speed was increased well beyond that of the flutter speed, the correlation was not as good. A possible explanation for this behavior is that the assumptions used to derive the von Kármán plate model might no longer be valid for the larger deflection levels that are encountered for the just-mentioned flow conditions.

In work on a similar delta-wing configuration, Gordnier[5] studied the LCO of a cropped flat-plate delta wing. In this study the structural theory was also the von Kármán model, but a finite element solution of this model was used. The structural model was combined with a Navier–Stokes computational-fluid-dynamic model to study the LCO for the wing at zero angle of attack and at Mach numbers ranging from 0.86 to 0.87. For these flow conditions the aerodynamic nonlinearities were weak, and the main nonlinearity was found to be caused by the structure. In this study, as was the case with the work by Attar and Tang, the LCO magnitudes were underpredicted for dynamic pressures above that of the flutter dynamic pressure.

In the current work, a high-fidelity, commercial finite element code (ANSYS[6]) is used as the structural model. This code uses the finite element form of the Rayleigh–Ritz method and the principle of virtual work to derive the nonlinear structural equations of motion. The aeroelastic behavior of a 45-deg delta wing is then modeled by coupling this structural model to a three-dimensional linear vortex lattic aerodynamic model.

The contributions of this work are the following. It will demonstrate improved theoretical and experimental correlations of LCO and flutter results when the higher-fidelity structural model is used in place of the von Kármán model. Theoretical LCO magnitude and flutter boundary predictions for a flat-plate delta wing at zero and nonzero angles of attack in low subsonic flow using both the higher-fidelity structural model and a von Kármán plate model will be compared to the experiment.

II. Theory

The delta-wing model studied is shown in Fig. 1. Results for two different structural models will be presented in this paper. The theory for the von Kármán plate model will not be presented here. See Dowell[7] for a theoretical development of the von Kármán model.

An abbreviated discussion is presented here for the higher-fidelity structural theory used in the development of the equations of motion used in the ANSYS software. To view a complete theoretical development of these equations, see the theory section of Ref. 6.

A. Structural Modeling

In this work a high-fidelity structural model was constructed using the ANSYS software package. This software package uses the finite element form of the Rayleigh–Ritz method to transform the nonlinear partial differential equations of motion to a set of nonlinear ordinary differential equations. In the work to be presented here, geometric structural nonlinearity will be considered, and the material will be assumed to be linearly elastic and isotropic. Also because the model that is to be examined is a thin plate, a state of plane stress is assumed. The theory that will be shown next will be derived at the element level. For a discussion of the theory on the assembly of the global stiffness matrix for the entire structure, please refer to Cook et al.[8]

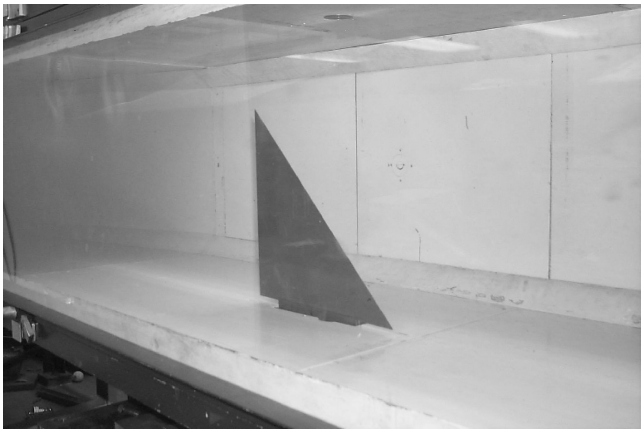

Fig. 1 Photograph of the delta-wing plate model in the wind tunnel.

Using the preceding assumptions, the stress–strain relationships are defined as

$$\varepsilon_x = \sigma_x/E - \nu\sigma_y/E \tag{1}$$

$$\varepsilon_y = -\nu\sigma_x/E + \sigma_y/E \tag{2}$$

$$\gamma_{xy} = \tau_{xy}/G \tag{3}$$

The principle of virtual work is most often used to derive the structural matrices when using the finite element method. The principle of virtual work states that the increment in strain energy caused by any admissible virtual displacement of the structure must be equal to the increment of work done by external forces such as body loads or surface tractions. This statement can be written as

$$\delta U = \delta W \tag{4}$$

$$\delta U = \int \{\delta\varepsilon\}^T \{\boldsymbol{\sigma}\}\, \mathrm{d}V \tag{5}$$

$$\delta W = \int \{\delta\boldsymbol{u}\}^T \{\boldsymbol{F}_b\}\, \mathrm{d}V + \int \{\delta\boldsymbol{u}\}^T \{\boldsymbol{F}_t\}\, \mathrm{d}S \tag{6}$$

where $\{\boldsymbol{u}\}$ is the vector of displacements. Using Eqs. (1–3), (5), and (6), Eq. (4) can be rewritten in the following manner:

$$\int \{\delta\varepsilon\}^T [\boldsymbol{D}]\{\varepsilon\}\, \mathrm{d}V = \int \{\delta\boldsymbol{u}\}^T \{\boldsymbol{F}_b\}\, \mathrm{d}V + \int \{\delta\boldsymbol{u}\}^T \{\boldsymbol{F}_t\}\, \mathrm{d}S \tag{7}$$

where $\boldsymbol{D}$ is a 3×3 matrix, which is a function of E and G. The principal idea behind the finite element method is the assumption that the displacements $\{\boldsymbol{u}\}$ can be interpolated at the element level using shape functions that define the order of the interpolation. In the work presented here, a shell element is used (the shell63 element in ANSYS). This element uses a plane-stress, quadrilateral element with extra shape functions to model the in-plane (x and y) displacement of structure. The shape functions for the in-plane deflections u_x and u_y are defined as

$$u_x = \tfrac{1}{4}\big[u_x^i(1-s)(1-t) + u_x^j(1+s)(1-t) + u_x^k(1+s)(1+t) + u_x^l(1-s)(1+t) + u_x^{es1}(1-s^2) + u_x^{es2}(1-t^2)\big] \tag{8}$$

$$u_y = \tfrac{1}{4}\big[u_y^i(1-s)(1-t) + u_y^j(1+s)(1-t) + u_y^k(1+s)(1+t) + u_y^l(1-s)(1+t) + u_y^{es1}(1-s^2) + u_y^{es2}(1-t^2)\big] \tag{9}$$

where i, j, k, and l indicate nodal displacements at the corresponding i, j, k, and l nodes of the four-noded element. The degrees

of freedom with superscripts $es1$ and $es2$ are nodeless degrees of freedom used to combat shear locking, which can occur in quadrilateral plane-stress elements. These extra shape functions are not used when forming the additional element stiffness caused by stress stiffening or the element mass matrix. In Eqs. (8) and (9), s and t are the local element coordinates. Triangular elements are formed by defining duplicate k and l nodes and deleting the extra shape functions so that the membrane stiffness reduces to a constant strain formulation.

The shape functions used for the out-of-plane deflection u_z and two rotations θ_x and θ_y are not explicitly defined in the code, as bending for this element is modeled using the discrete Kirchhoff element. The in-plane rotational(drilling) degree of freedom θ_z has no stiffness associated with the shape functions. However a small stiffness is added for this degree of freedom to prevent numerical instability. See Ref. 8 for a theoretical development of this element.

The strains are related to the displacements via the strain-displacement relationships:

$$\{\varepsilon\} = [\boldsymbol{B}]\{\boldsymbol{u}\} \tag{10}$$

In Eq. 10 $[\boldsymbol{B}]$ is the strain-displacement matrix in the orginal element coordinate system. This is a function of the type of element used and the strain-displacement relationships used. Because the element that is used in the work presented here has both axial and bending stiffness, the small displacement form of these strain-displacement relationships can be written in the following manner:

$$\varepsilon_x = \frac{\partial u_x}{\partial x} - z\frac{\partial^2 u_z}{\partial x^2} \tag{11}$$

$$\varepsilon_y = \frac{\partial u_y}{\partial y} - z\frac{\partial^2 u_z}{\partial y^2} \tag{12}$$

$$\gamma_{xy} = \frac{\partial u_x}{\partial x} + \frac{\partial u_y}{\partial y} - 2z\frac{\partial^2 u_z}{\partial x \partial y} \tag{13}$$

If Eqs. (1–3), (5), and (10) are combined, the virtual strain energy δU can be written in the following manner:

$$\delta U = \{\delta \boldsymbol{u}\}^T \int [\boldsymbol{B}]^T [\boldsymbol{D}][\boldsymbol{B}]\,\mathrm{d}V\{\boldsymbol{u}\} \tag{14}$$

The virtual work caused by inertia effects δW^i can be written as

$$\delta W^i = -\{\delta \boldsymbol{u}\}^T \rho \int [\boldsymbol{N}]^T [\boldsymbol{N}]\,\mathrm{d}V \frac{\delta^2}{\delta t^2}\{\boldsymbol{u}\} \tag{15}$$

where $[\boldsymbol{N}]$ is the matrix of shape functions. To couple the aerodynamic model to the structural model, pressure is applied to structure. The virtual work as a result of applied pressure is written as

$$\delta W^p = \{\delta \boldsymbol{u}\}^T \int [\boldsymbol{N}_n]\{\boldsymbol{P}\}\,\mathrm{d}S \tag{16}$$

In Eq. 16, $[\boldsymbol{N}_n]$ is a matrix of shape functions that are defined to be normal to the element area $\mathrm{d}S$ and $\{\boldsymbol{P}\}$ is a vector of applied pressure.

Combining Eqs. (7), (14–16) gives the following relationship for the principle of virtual work:

$$\{\delta \boldsymbol{u}\}^T \int [\boldsymbol{B}]^T [\boldsymbol{D}][\boldsymbol{B}]\,\mathrm{d}V\{\boldsymbol{u}\} = -\{\delta \boldsymbol{u}\}^T \rho \int [\boldsymbol{N}]^T [\boldsymbol{N}]\,\mathrm{d}V \frac{\delta^2}{\delta t^2}\{\boldsymbol{u}\}$$

$$+ \{\delta \boldsymbol{u}\}^T \int [\boldsymbol{N}_n]\{\boldsymbol{P}\}\,\mathrm{d}S \tag{17}$$

Because the vector of virtual displacements $\{\delta \boldsymbol{u}\}^T$ is arbitrary, the conditions needed to satisfy Eq. (17) reduce to the following:

$$[\boldsymbol{K}]\{\boldsymbol{u}\} = -[\boldsymbol{M}]\{\ddot{\boldsymbol{u}}\} + \{\boldsymbol{F}^P\} \tag{18}$$

$$[\boldsymbol{K}] = \int [\boldsymbol{B}]^T [\boldsymbol{D}][\boldsymbol{B}]\,\mathrm{d}V \tag{19}$$

$$[\boldsymbol{M}] = \rho \int [\boldsymbol{N}]^T [\boldsymbol{N}]\,\mathrm{d}V \tag{20}$$

$$\{\boldsymbol{F}^P\} = \int [\boldsymbol{N}_n]\{\boldsymbol{P}\}\,\mathrm{d}S \tag{21}$$

where $[\boldsymbol{K}]$ is the element stiffness matrix, $[\boldsymbol{M}]$ is the element mass matrix, and $\{\boldsymbol{F}^P\}$ is the element load vector caused by pressure.

Two types of geometric nonlinearity will be included in this work. The first is caused by large rotations of a structure. The second is caused by the coupling of the in-plane and out-of-plane deflection. The geometric nonlinearity caused by out-of-plane and in-plane coupling is often referred to as stress stiffening.

The large rotation capability is modeled using a corotational approach. In this method, a local coordinate system is attached to each element, which translates and rotates with the element as deformation takes place. The original element coordinate system stays fixed, and the element deformation can therefore be decomposed into a rigid-body component and a component that induces strain. In matrix form this can be written in the following manner:

$$[\boldsymbol{B}_l] = [\boldsymbol{B}][\boldsymbol{T}_l] \tag{22}$$

where $[\boldsymbol{B}_l]$ is the strain-displacement matrix written in the local, convected coordinate system and $[\boldsymbol{T}_l]$ is an orthogonal transformation matrix, which relates the original element coordinates to the convected element coordinates. The stress stiffness capability in ANSYS is modeled using the nonlinear Green strain-displacement relationships:

$$\varepsilon_x = \frac{\partial u_x}{\partial x} + \frac{1}{2}\left[\left(\frac{\partial u_x}{\partial x}\right)^2 + \left(\frac{\partial u_y}{\partial x}\right)^2 + \left(\frac{\partial u_z}{\partial x}\right)^2\right] \tag{23}$$

$$\varepsilon_y = \frac{\partial u_y}{\partial y} + \frac{1}{2}\left[\left(\frac{\partial u_x}{\partial y}\right)^2 + \left(\frac{\partial u_y}{\partial y}\right)^2 + \left(\frac{\partial u_z}{\partial y}\right)^2\right] \tag{24}$$

$$\gamma_{xy} = \frac{\partial u_x}{\partial y} + \frac{\partial u_y}{\partial x} + \frac{\partial u_x}{\partial x}\frac{\partial u_x}{\partial y} + \frac{\partial u_y}{\partial x}\frac{\partial u_y}{\partial y} + \frac{\partial u_z}{\partial x}\frac{\partial u_z}{\partial y} \tag{25}$$

Note that Eqs. (23–25) correspond to a Lagrangian description that refers to the original element coordinate system.

In practice, when large rotation and stress stiffness are to be included using the shell63 element the ANSYS software computes the element tangent stiffness matrix $[\boldsymbol{K}]$ using a consistent approach. This approach was originally developed by Nour-Omid and Rankin.[9] The description of this method given here follows that of the ANSYS theory document.

The elemental force vector caused by strain energy can be written as the gradient of elemental strain energy U with respect the displacements $\{\boldsymbol{u}\}$:

$$\{\boldsymbol{F}_{\text{int}}\} = \frac{\partial U}{\partial \{\boldsymbol{u}\}} = \int [\boldsymbol{B}]^T \{\boldsymbol{\sigma}\}\,\mathrm{d}V \tag{26}$$

The consistent tangent stiffness matrix, in the original element coordinates, can now be computed by taking the derivative with respect to the displacements of Eq. (26) rotated to the original element coordinate system:

$$[\boldsymbol{K}]^T_{\text{consistent}} = [\boldsymbol{T}_l]^T \frac{\partial\{\boldsymbol{F}_{\text{int}}\}}{\partial\{\boldsymbol{u}\}} + \frac{\partial[\boldsymbol{T}_l]^T}{\partial\{\boldsymbol{u}\}}\{\boldsymbol{F}_{\text{int}}\} = [\boldsymbol{T}_l]^T \int [\boldsymbol{B}]^T \frac{\partial\{\boldsymbol{\sigma}\}}{\partial\{\boldsymbol{u}\}}\,\mathrm{d}V$$

$$+ [\boldsymbol{T}_l]^T \int \frac{\partial[\boldsymbol{B}]^T}{\partial\{\boldsymbol{u}\}}\,\mathrm{d}V + \frac{\partial[\boldsymbol{T}_l]^T}{\partial\{\boldsymbol{u}\}} \int [\boldsymbol{B}]^T \{\boldsymbol{\sigma}\}\,\mathrm{d}V \tag{27}$$

The first term in Eq. (27) is the main tangent stiffness matrix. The second integral is caused by stress stiffening and is computed using the stress state from the previous iteration in a Newton–Raphson procedure. These stresses are computed using the Green strain-displacement terms in Eq. (23–25), which augment the small-displacement relations given in Eqs. (11–13). The final integral is

also caused by stress stiffening, and including it usually increases the rate of convergence of the Newton–Raphson iteration.

Now using the consistent stiffness matrix formulation, the structural equations of motion at the element level become

$$[\boldsymbol{M}]\{\ddot{\boldsymbol{u}}\} + [\boldsymbol{C}]\{\dot{\boldsymbol{u}}\} + [\boldsymbol{K}]_{\text{consistent}}\{\boldsymbol{u}\} = \{\boldsymbol{F}^P\} \tag{28}$$

where the damping matrix is defined as

$$[\boldsymbol{C}] = \beta[\boldsymbol{K}]_{\text{consistent}} \tag{29}$$

where β is a constant. Equation (28) is integrated forward in time using the constant acceleration form of the Newmark method and a Newton–Raphson iteration.

B. Differences Between the von Kármán Theory and Corotational Theory

As was stated in the preceding theoretical discussion, in the corotational theory the displacements of a structure are decomposed into a rigid-body portion and a pure deformation portion, which induces strain in the model. If the element size does not change substantially with deflections, when the rigid-body portion is subtracted from the full displacement the portion that is left can be assumed to be small in comparison to the element dimension. Therefore a small strain assumption can be assumed, and linear strain-displacement relationships can be used to compose the element tangent stiffness matrix in the local coordinate system. The coordinate transformation from the local coordinate to the global coordinate system introduces the displacement dependent stiffness through the transformation matrices, which are functions of the displacement of the element. Only in cases of extreme deformation where element size would change substantially with deflection, such as the inflation of a balloon, are nonlinear Green strain-displacement relationships needed in the formation of the tangent stiffness matrix. In the work presented here the nonlinear strain displacements are included in the evaluations of the second and third integrals in Eq. (27); however, the main reason they are included is to increase the speed of convergence of the solution to the nonlinear system of equations.[9] In this work, the final answer is not affected by the use of the nonlinear Green strain-displacement relationships.

In the von Kármán model a total Lagrangian frame is used, and the total displacement is assumed to cause strain. This results in the use of the full displacement in the nonlinear von Kármán strain-displacement relationships. The von Kármán strain-displacement relationships are a degenerated form of the Green strain-displacement relationships with the higher-order nonlinear membrane terms $[(\partial u_x/\partial y)^2,\ (\partial u_y/\partial y)^2,$ etc.] deleted from Eqs. (23–25). Although the use of the nonlinear strain-displacement relationships is not necessary for the corotational formulation if the large rotation/displacement, small strain assumption is valid, it appears that a total Lagrangian method needs to include not only the nonlinear bending terms in the strain-displacement relationships but also the nonlinear membrane terms if large rotation is to be modeled correctly. Total Lagrangian methods that use Green strain have been shown to give results comparable to those using the corotational theory for problems involving large rotation.[10] The work in Ref. 10 also demonstrated that if a total Lagrangian frame of reference is to be used with the Green strain the spatial discretization of the in-plane equations must be of high order. This is somewhat surprising because the in-plane displacement field would appear to be of lower order because the equations of motion that govern it are second-order equations. In fact most shell elements use different order shape functions to represent the membrane and transverse displacement fields, with the transverse displacement modeled using a higher-order shape function. A possible explanation for this result was given in Ref. 11. In this paper it was noted that in Lagrangian formulations as an element of the structure rotates a portion of the transverse displacement becomes axial. For example in a beam, if the element rotates 90 deg, the linear axial displacement field will be normal to the element plane, while the cubic transverse displacement field will be along the element axis. This then requires the modeling of the axial displacement to be of the same order as the transverse displacement.

In problems where the applied load is carried predominantly by the in-plane stresses, such as a square plate clamped on all four sides, the von Kármán approximation is able to model the physics accurately as the results from a von Kármán model and a corotational model have been shown to be comparable.[12] This type of problem is the typical type of problem for which the von Kármán model has been used in the past several decades.[7] Apparently for problems such as these the additional terms from a Green strain-displacement formulation do not contribute substantially to the model accuracy.

C. Aerodynamic Modeling

The flowfield about the delta-wing model is assumed to be a potential flow. Therefore the equations of motion for the fluid can be reduced to Laplace's equation

$$\nabla^2\Phi = 0 \tag{30}$$

The boundary conditions that must be satisfied are that of zero normal flow on the wing, that is,

$$(\nabla\Phi + \boldsymbol{q}) \cdot \boldsymbol{n} = 0 \tag{31}$$

and also that the disturbance created by the potential must decay at distances far from the wing. The latter can be expressed as

$$\lim_{r\to\infty} \nabla\Phi = 0 \tag{32}$$

where $\boldsymbol{q}$ is the relative velocity between the undisturbed fluid in the fluid domain and the wing. Using Green's identity, it can be shown[13] that a solution to Eq. (30) can be found by distributing elementary solutions to Laplace's equation on the problem boundaries. For the model presented here, this is accomplished by distributing vortex rings on the wing surface and in the wake.

If the solid boundary of the wing is defined as

$$F(x, y, z, t) = z - \eta(x, y, t) = 0 \tag{33}$$

then the zero normal flow boundary condition, Eq. (31), can be expressed as

$$\frac{\mathrm{D}F}{\mathrm{D}t} = \frac{\partial F}{\partial t} + -\boldsymbol{U}_\infty \cdot \nabla F + \nabla\Phi \cdot \nabla F = 0 \tag{34}$$

where $\boldsymbol{U}_\infty$ is the freestream velocity of the wing as viewed from the inertial frame. For the thin surface with zero initial curvature considered here, $\eta(x, y, t)$ is the out-of-plane structural deformation of the surface

$$\eta(x, y, t) = u_z(x, y, t) \tag{35}$$

If the small disturbance approximation to the aerodynamic boundary condition is used along with Eq. (35), Eq. (34) can be rewritten in the following form:

$$\frac{\partial\Phi}{\partial z} = |\boldsymbol{U}_\infty|\left(\alpha - \frac{\partial u_z}{\partial x}\right) + \frac{\partial u_z}{\partial t} \tag{36}$$

where the angle α is the angle the freestream velocity $\boldsymbol{U}_\infty$ makes with the undeformed wing and $|\boldsymbol{U}_\infty|$ denotes the magnitude of the freestream flow velocity vector.

The flow model is solved by placing vortex rings on the wing and in the wake.[1–3,14] The wake is assumed to be planar so that the force-free wake condition is not imposed. This is usually a valid assumption for simulations involving the translation of a fixed wing, and using this assumption dramatically increases the computational efficiency of the model. The resulting model can be expressed in matrix form as

$$[\boldsymbol{A}_b]\{\boldsymbol{\Gamma}_b\}^{n+1} = [\boldsymbol{ET}]\left\{\frac{\partial \boldsymbol{u}_z}{\partial t}\right\}^{n+\frac{1}{2}} + |\boldsymbol{U}_\infty|[\boldsymbol{ET}]\left\{\frac{\partial \boldsymbol{u}_z}{\partial x}\right\}^{n+\frac{1}{2}} + |\boldsymbol{U}_\infty|\{\boldsymbol{\alpha}\} - [\boldsymbol{A}_w]\{\boldsymbol{\Gamma}_w\}^n \tag{37}$$

where $[\boldsymbol{A}_b]$ is the influence coefficient matrix for the influence of the wing bound circulation at the wing collocation points, $[\boldsymbol{A}_w]$ is the influence coefficient matrix for the influence of the wake circulation at the wing collocation points, and $\{\boldsymbol{\Gamma}_b\}$ and $\{\boldsymbol{\Gamma}_w\}$ are the vectors of bound and wake circulation, respectively. Also the superscripts n, $n+\frac{1}{2}$, and $n+1$ represent the time steps in the time integration, where $n+\frac{1}{2}$ represents an intermediate step during the fluid-structure inner iteration. Finally $\boldsymbol{ET}$ is a matrix that interpolates the displacements u_z from the structural model nodes to the aerodynamic model collocation points. This interpolation is done with a thin-plate spline. See Katz and Plotkin[15] for details on the use of vortex rings to discretize the flow model.

The pressure on the wing is computed using the unsteady form of Bernoulli's equation:

$$\frac{p_\infty - p}{\rho_\infty} = \frac{(\nabla\Phi)^2}{2} - \left(\boldsymbol{U}_\infty + \frac{\partial u_z}{\partial t}\right)\cdot\nabla\Phi + \frac{\partial\Phi}{\partial t} \tag{38}$$

D. Aeroelastic Modeling

To model the aeroelastic phenomena, the structural model and aerodynamic model must be coupled. In the structural equation, Eq. (28), this coupling is caused by the pressure load vector $\{F^P\}$. In the aerodynamic system, the coupling comes from the x and t derivatives of the out-of-plane deflection u_z in the zero through-flow aerodynamic boundary condition equation (36). So to couple the two physics models, both pressure and displacements must be transferred between the aerodynamic model and structural model. This transfer is accomplished by the user programmable features of ANSYS (UPF), which supply subroutines for transferring data between the ANSYS code and third-party software.

Because the aerodynamic and structural meshes are not necessarily the same, the displacement, velocity, and pressure must be interpolated from one mesh to the other. In the work presented here, the velocities and displacements are interpolated from the structural mesh to the aerodynamic mesh using a thin-plate spline routine. The pressures are interpolated by finding the best triangle of points on the aerodynamic mesh that contains the structural mesh node to which the pressure value is to be interpolated and then using linear interpolation inside this triangle.

Each time step begins with the prediction of the structural displacement and structural velocity using a Taylor series. These predicted values are used in Eq. (37), and the bound circulation on the wing can then be calculated. Using this circulation, the pressure distribution on the wing can be determined using Eq. (38). This pressure is then passed to ANSYS, which calculates new displacements and velocities. The procedure of recalculating pressure, displacements, and velocities is continued until the difference in the values for each of the transferred quantities is less than some prescribed tolerance for two successive iterations. Once this is accomplished, the wake is convected, and a new time step is taken.

III. Results

The delta-wing model studied here is a 45-deg delta wing constructed out of 1.6-mm-thick Plexiglas®. The root-chord and trailing-edge span dimensions both measure 0.381 m, and the root chord is fixed to the wind-tunnel wall along the middle 60% of its length. All other boundaries are free. The modulus of elasticity of the material was taken to be 3.3 GPa, and the material density used in the modeling was 1299 kg/m^3. The density of air was taken to be 1.225 kg/m^3.

The aerodynamic model was constructed using 900 vortex rings on the wing, and four-wing chords of wake were kept in the model. The time step used to integrate the aerodynamic equations of motion forward in time was 5.0×10^{-4} s.

The structural model was constructed using 552 shell elements containing 614 nodes. These elements have six degrees of freedom per node. The structural grid used is shown in Fig. 2. In the experimental model the middle 60% of root chord is fixed. Because completely constraining all rotations and translations in an experimental model is not possible, in the numerical modeling two sets of

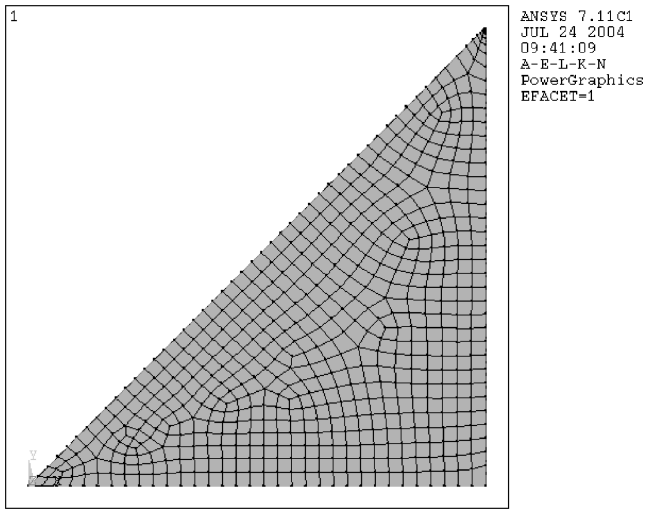

Fig. 2 Grid used in the computational structural model.

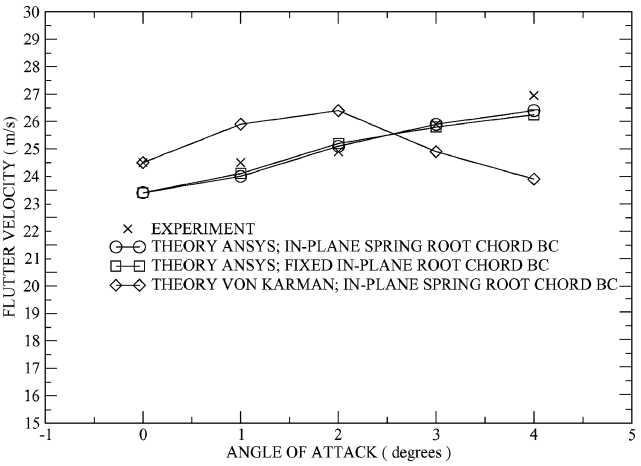

Fig. 3 Delta-wing flutter velocity as a function of the mean flow angle of attack.

in-plane boundary conditions are examined. The first type uses stiff linear springs so that the two displacements u_x and u_y and rotation about the z axis, θ_z are allowed some movement. The out-of-plane displacement u_z and rotations about the x and y axes are fixed along this length. The second type is a fully fixed boundary condition, which constrains all of the nodal degrees of freedom along the partial clamped wing root edge.

The time step used in the structural model was 3.3×10^{-5} s. Fluid-structure subiterations were used to reduce the error caused by the loose coupling of the fluid and structure. Typically only three to six fluid-structure subiterations were needed to achieve convergence of the displacement, velocity, and pressure results.

The experimental responses were measured in the Duke University low-speed wind tunnel using an accelerometer. The Labview software program[16] was used for data acquisition. The accelerometer was placed at the tip of the delta-wing model.

Figures 3 and 4 show the flutter velocity and flutter frequency as a function of the steady flow angle of attack. Three sets of theoretical results are shown on the plot along with experimental results. The experimental flutter point was determined by examining fast Fourier transforms of the wing response at various flow velocities and determining when the response contained one dominant response frequency (flutter frequency). The results calculated using the high-fidelity model show better qualitative and quantitative correlation with experiment than do the results calculated using the von Kármán model. Also note that the results found using the high-fidelity model do not show a great sensitivity with respect to the type of root-chord in-plane boundary condition used in the

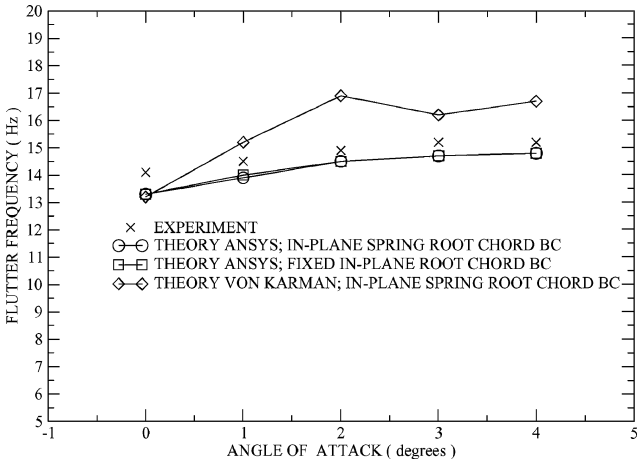

Fig. 4 Delta-wing flutter frequency as a function of the mean flow angle of attack.

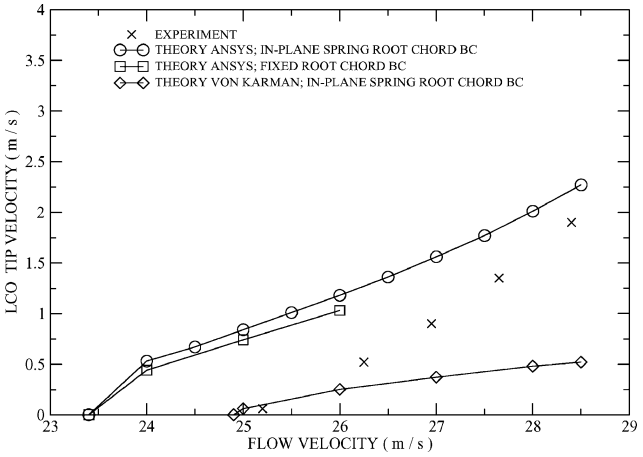

Fig. 5 Delta-wing LCO tip velocity vs mean flow velocity: angle of attack of 0 deg.

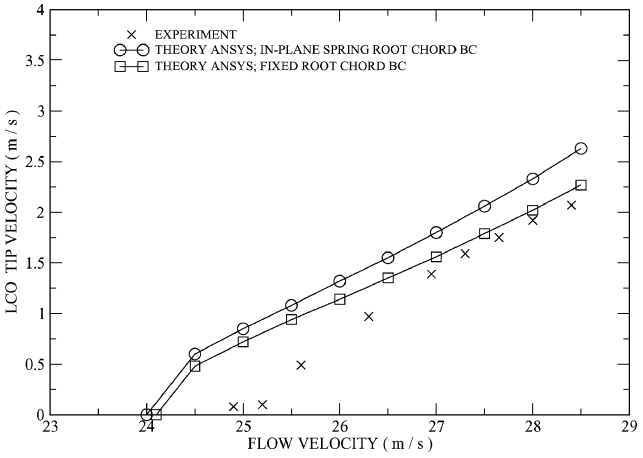

Fig. 6 Delta-wing LCO tip velocity vs mean flow velocity: angle of attack of 1 deg.

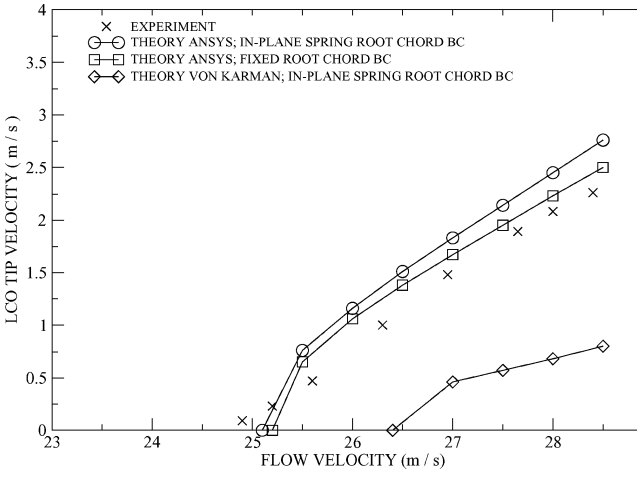

Fig. 7 Delta-wing LCO tip velocity vs mean flow velocity: angle of attack of 2 deg.

model. This is not the case for the von Kármán model. The flutter velocities found using the von Kármán model with a fixed boundary, which are not shown in Figs. 3 and 4, are $\boldsymbol{U}_\infty = 36$ m/s for a 1-deg angle of attack and $\boldsymbol{U}_\infty = 57$ m/s for a 2-deg angle of attack. The corresponding flutter frequencies are 42.5 and 114.0 Hz. For angles of attack greater than 2 deg, the von Kármán model with the fixed in-plane boundary conditions predicted flutter speeds above 100 m/s. The theoretical nonzero angle-of-attack results predicted using the von Kármán model with fixed boundary conditions clearly do not model the physical phenomena correctly and thus in Figs. 3 and 4 show that von Kármán results are presented only for the computational model, which uses the in-plane spring boundary condition.

The large quantitative and qualitative discrepancies between the nonzero angle-of-attack experimental flutter parameter results and the nonzero angle of attack theoretical von Kármán flutter parameter results can be explained in the following manner. The flutter speed in the coalescence-type flutter of this system is determined mainly by the separation in the structural response frequencies of the first bending and first torsion modes. At a nonzero angle of attack, a change in model stiffness occurs as a result of the static deformation of the wing caused by the static-pressure difference. This change in stiffness is a nonlinear effect. If this stiffness change is such that the difference in the first bending and first torsion frequencies is larger then the difference predicted by a linear structural model, the flutter velocity will be above that of the flutter velocity predicted by a linear model. If the stiffness change is such that the difference is decreased, then the flutter speed will be lower than that which would be predicted using a linear structural model. The fact that the von Kármán model does not adequately reproduce the flutter vs angle-of-attack curve would appear to show that the change in the model stiffness is not modeled correctly using the von Kármán theory. The reasoning behind this can be explained using the ideas laid out in Sec. II.A.1.

Figures 5–9 are plots of the delta-wing out-of-plane tip velocity LCO results for five angles of attack, 0, 1, 2, 3, and 4 deg. Limit-cycle results computed using the high-fidelity model are shown for all five angles of attack and both types of in-plane boundary conditions. Results computed using the von Kármán model are shown for 0-, 2-, and 4-deg angles of attack. Results from the lower-fidelity structural model, von Kármán plate theory have not been computed for two of the angles of attack, that is, 1 and 3 deg, because clearly this model is not as accurate as the higher-fidelity structural model for the present application. The computed results are compared to the experimental data. For all angles of attack, the correlation of the high-fidelity model results, and experiment is very good and is markedly better than those computed using the von Kármán model. The qualitative shape of the LCO curves predicted by the high-fidelity model is more comparable to the experimental result, which shows a near linear increase in LCO magnitude with flow velocity. Quantitatively, the computed LCO magnitudes from the higher-fidelity model are much closer to those of experiment. Although the results computed using the aeroelastic model that uses the high-fidelity theory do not show a great sensitivity to the type of in-plane boundary conditions used, the small differences that are present appear to decrease as the angle of attack increases.

Figures 10–14 show the LCO frequency as a function of flow velocity for the same five angles of attack. Once again the results computed using high-fidelity model show good agreement with

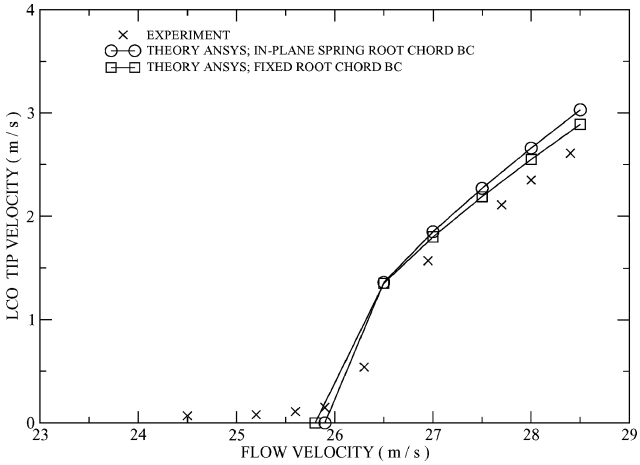

Fig. 8 Delta-wing LCO tip velocity vs mean flow velocity: angle of attack of 3 deg.

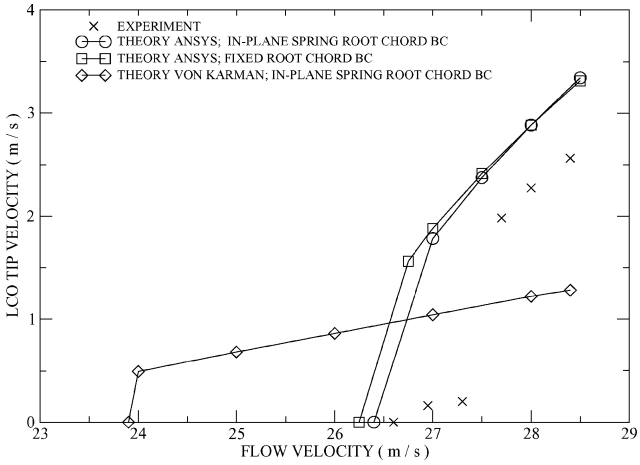

Fig. 9 Delta-wing LCO tip velocity vs mean flow velocity: angle of attack of 4 deg.

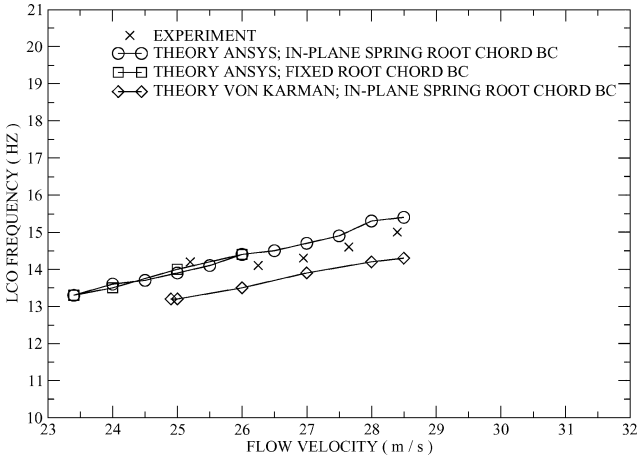

Fig. 10 Delta-wing LCO frequency vs mean flow velocity: angle of attack of 0 deg.

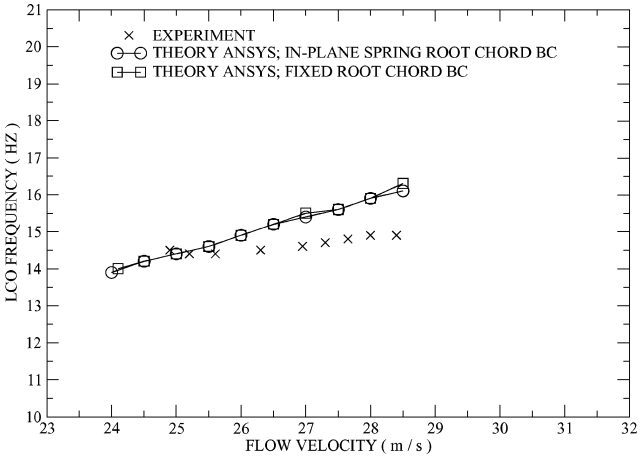

Fig. 11 Delta-wing LCO frequency vs mean flow velocity: angle of attack of 1 deg.

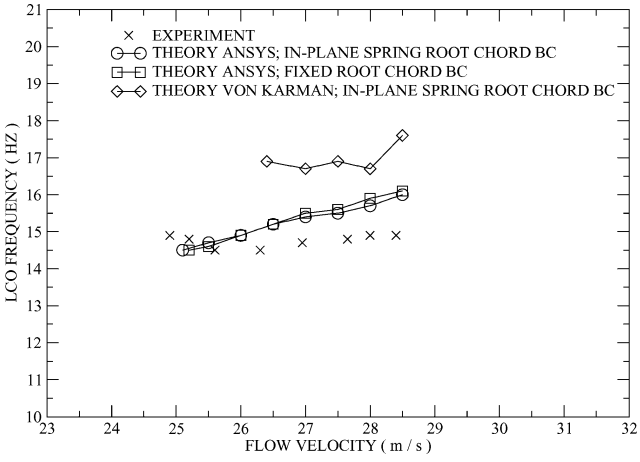

Fig. 12 Delta-wing LCO frequency vs mean flow velocity: angle of attack of 2 deg.

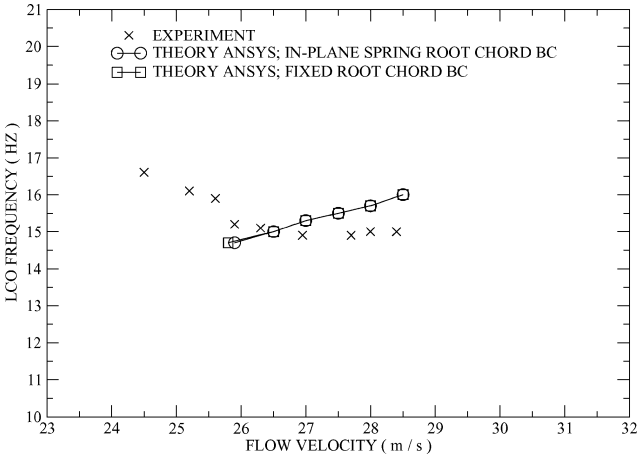

Fig. 13 Delta-wing LCO frequency vs mean flow velocity: angle of attack of 3 deg.

the experimental data. The LCO frequency appears to be a very weak function of the flow velocity, and this is predicted by both the high-fidelity and von Kármán structural models. From a quantitative standpoint, the high-fidelity model does a better job at predicting the LCO frequency results then does the von Kármán model.

Figures 15–17 display the LCO tip velocity normalized by the product of the LCO circular frequency and wing thickness. This parameter can be thought of as a measure of the out-of-plane tip deflection normalized by the thickness u_z/h. These values are plotted as a function of flow velocity for three angles of attack, 0, 2, and 4 deg. These figures present results for three different theoretical calculations and the experimental data. The LCO frequency used in the normalization is the corresponding LCO frequency for the given angle of attack and flow velocity. One thing to note in Figs. 15–17 is the large LCO magnitudes that are present in the experiment and that are predicted by the computational model, which uses the high-fidelity theory. For nonzero angles of attack, the wing

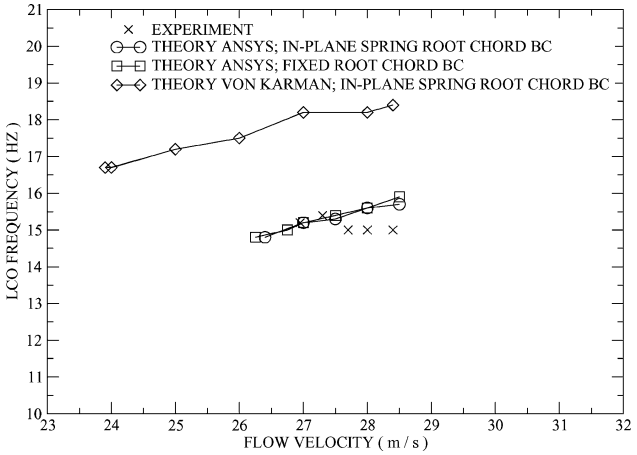

Fig. 14 Delta-wing LCO frequency vs mean flow velocity: angle of attack of 4 deg.

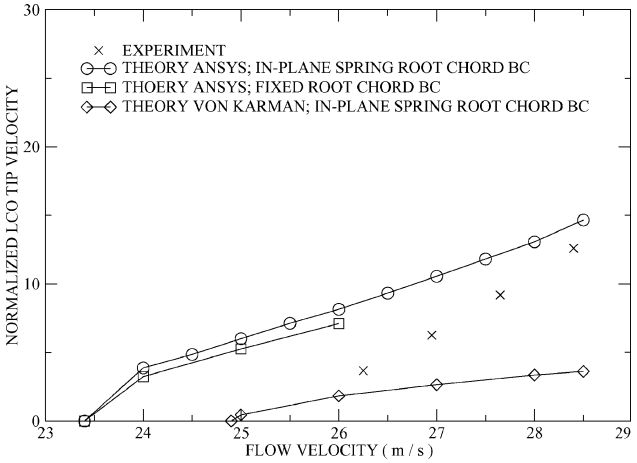

Fig. 15 Delta-wing tip LCO velocity normalized by the product of LCO frequency and wing thickness: angle of attack of 0 deg.

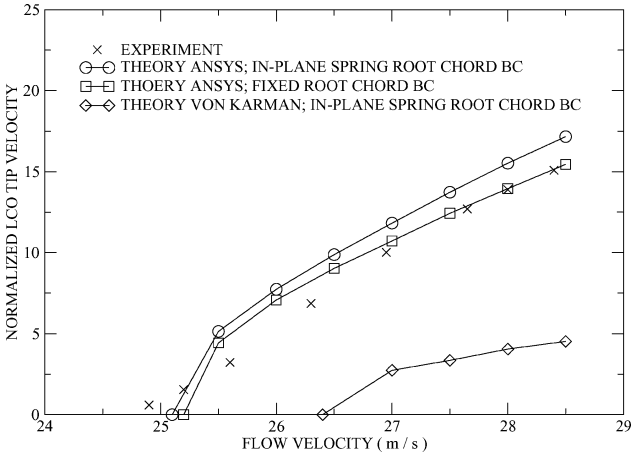

Fig. 16 Delta-wing tip LCO velocity normalized by the product of LCO frequency and wing thickness: angle of attack of 2 deg.

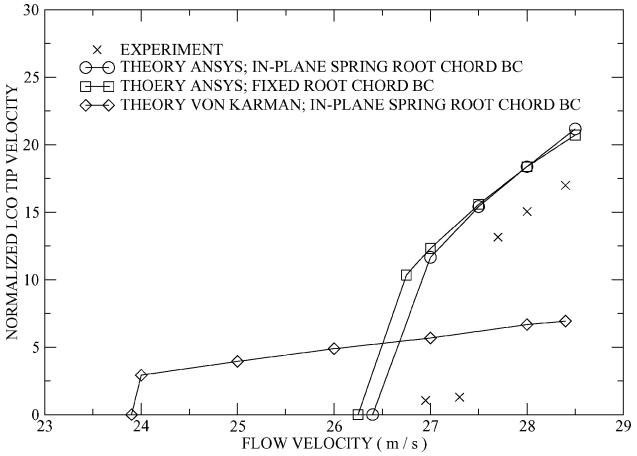

Fig. 17 Delta-wing tip LCO velocity normalized by the product of LCO frequency and wing thicknes: angle of attack of 4 deg.

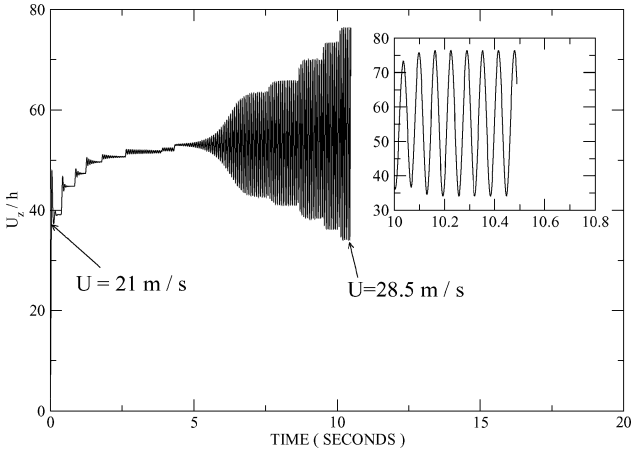

Fig. 18 Delta-wing out-of-plane tip LCO (u_z/h) plotted as a function of time as computed by the aeroelastic model, which uses the high-fidelity structural theory. Wing is placed at an angle of attack of 4 deg, and the flow speed is increased from 21 m/s to 28.5.

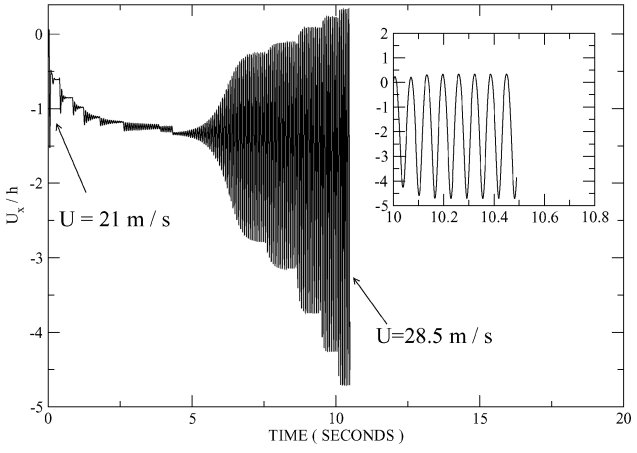

Fig. 19 Delta-wing in-plane tip LCO (u_x/h) plotted as a function of time as computed by the aeroelastic model, which uses the high-fidelity structural theory. Wing is placed at an angle of attack of 4 deg, and the flow speed is increased from 21 m/s to 28.5.

actually oscillates about a nonzero static deflection so that the absolute deflection magnitudes are even larger than what is shown in the figures. A typical time history computed using the aeroelastic model that uses the high-fidelity structural model is shown in Fig. 18. In this figure one can see the total deflection (static deflection plus LCO magnitude) that is computed using the high-fidelity model. Note the wing has an angle of attack at the root of 4 deg, and the fixed in-plane root chord boundary condition is used. In Fig. 18 the out-of-plane tip deflection u_z of the delta wing normalized by the thickness is plotted vs a dimensional time. In the figure the flow speed is increased from 21 m/s, which is approximately 20% below the predicted flutter speed, to 28.5 m/s, which is about 5% above the predicted flutter speed. Figures 19 and 20 are the corresponding time histories for the normalized (by the thickness) x and y deflections u_x and u_y. Note that in Figs. 18–20 the time simulation is run until the transient dynamics have decayed to a steady-state LCO before the flow velocity is increased further.

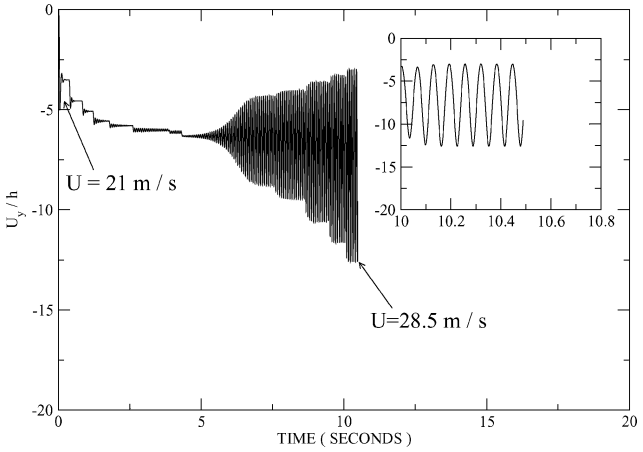

Fig. 20 Delta-wing in-plane tip LCO (u_y/h) plotted as a function of a time as computed by the aeroelastic model, which uses the high-fidelity structural theory. Wing is placed at an angle of attack of 4 deg, and the flow speed is increased from 21 m/s to 28.5.

An interesting result from Figs.19 and 20 is that the frequency of in-plane vibration is approximately the same as that of the out-of-plane motion. In von Kármán theory, because the dominant nonlinearity is caused by the in-plane and out-of-plane coupling, the in-plane vibrational frequency is predicted to be twice that of the out-of-plane vibration. Unfortunately measurements of the in-plane vibration are not available.

IV. Conclusions

The flutter and limit-cycle-oscillation (LCO) behavior of a delta wing are studied with an aeroelastic model, which uses a high-fidelity structural model. Results are computed for the wing placed at zero and nonzero angles of attack. The results from this model are compared to theoretical results computed using a lower-fidelity aeroelastic model and to experiment.

The flutter velocity and frequency computed using the high-fidelity aeroelastic model correlate well with experiment for all angles of attack studied and show improvement over those computed using the aeroelastic model, which uses von Kármán plate theory. Two separate root-chord in-plane boundary conditions are modeled computationally for both the high-fidelity model and the von Kármán model. Unlike those computed using an aeroelastic model, which uses von Kármán theory, the flutter (and LCO) results computed using the high-fidelity model do not show a sensitivity to these boundary conditions.

Postflutter LCO results were also computed using the high-fidelity theoretical model for the two separate in-plane boundary conditions and five different angles of attack. Theoretical LCO results were also computed using the von Kármán aeroelastic model for the in-plane spring root-chord boundary condition and for three angles of attack (0, 2, and 4 deg). For all angles of attack studied, the high-fidelity model results compare well with experiment and are considerably better then those computed using the lower-fidelity model. The LCO results computed using the high-fidelity model show a slight sensitivity to the type of in-plane root-chord boundary conditions used. Interestingly the small differences in the results for the two different boundary conditions that are seen appear to decrease as the angle of attack increases.

The results presented in this paper show the importance of using a high-fidelity structural model when modeling the LCO of cantilevered wings, which undergo moderate to large-amplitude LCO. In von Kármán theory caused by the total Lagrangian frame that is used, all displacement is assumed to cause strain. This appears to cause an overprediction of the in-plane forces as a result of displacement. It is thought that if the full Green strain-displacement relationships are used in place of the von Kármán model, large rotation will be handled correctly, and this overprediction of the in-plane/out-of-plane coupling will not occur. In this work the corotational model is used, which decomposes the total displacement into a rigid-body portion and a portion that causes strain. This transfers most of the nonlinearity to the coordinate transformation and allows linear strain-displacement relationships to be used.

Further work in the area of aeroelastic modeling could be done to couple the high-fidelity structural model used here to a high-fidelity aerodynamic model such that aeroelastic behavior could be studied for configurations, which also contain significant aerodynamic nonlinearities. Further investigations could also include a study of the effect of adding the deleted higher-order strain-displacement terms in the von Kármán model and comparing LCO results from a total Lagrangian, Green strain method to those computed using the corotational model in the present work.

Acknowledgment

This work was supported by Air Force Office of Scientific Research Grant "Dynamics and Control of Nonlinear Fluid-Structure Interaction" under the direction of Dean Mook and Captain Clark Allred.

References

[1]Tang, D., Henry, J., and Dowell, E., "Limit Cycle Oscillations of Delta Wing Models in Low Subsonic Flow," *AIAA Journal*, Vol. 37, No. 1, 1999, pp. 155–164.

[2]Tang, D., Dowell, E., and Hall, K., "Limit Cycle Oscillations of a Cantilevered Wing in Low Subsonic Flow," *AIAA Journal*, Vol. 37, No. 3, 1999, pp. 364–371.

[3]Attar, P., Dowell, E., and Tang, D., "Theoretical and Experimental Investigation of the Effects of a Steady Angle of Attack on the Nonlinear Flutter of a Delta Wing Plate Model," *Journal of Fluids and Structures*, Vol. 17, No. 2, 2003, pp. 243–259.

[4]Attar, P., Dowell, E., and Tang, D., "Modeling Aerodynamic Nonlinearities for Two Aeroelastic Configurations: Delta Wing and Flapping Flag," AIAA Paper 1402, April 2003.

[5]Gordnier, R., "Computation of Limit Cycle Oscillations of a Delta Wing," AIAA Paper 2002-1411, April 2002.

[6]ANSYS User Manual, Release 7.1 Swanson Analysis Systems, In., Cannonsburg, PA, 2002.

[7]Dowell, E., *Aeroelasticity of Plates and Shells*, Noordhoff, Leiden, The Netherlands, 1975, Chap. 3.

[8]Cook, R., Malkus, D., Plesha, M., and Witt, R., *Concepts and Applications of Finite Element Analysis*, 4th ed., Wiley, New York, 2002, Chap. 2.

[9]Nour-Omid, B., and Rankin, C., "Finite Rotation Analysis and Consistent Linearization Using Projectors," *Computer Methods in Applied Mechanics and Engineering*, Vol. 93, No. 3, 1991, pp. 353–384.

[10]Rankin, C., and Brogan, F., "An Element Independent Corotational Procedure for the Treatment of Large Rotations," *Journal of Pressure Vessel Technology*, Vol. 108, No. 2, May 1986, pp. 165–173.

[11]Belytschko, T., and Hsieh, B., "Non-Linear Transient Finite Element Analysis with Convected Co-Ordinates," *International Journal for Numerical Methods in Engineering*, Vol. 7, No. 3, 1973, pp. 255–271.

[12]Jiang, J., and Olson, M., "Large Elastic-Plastic Deformations of Slender Beams: Co-rotational Theory vs. von Karman Theory," *Computational Mechanics*, Vol. 15, No. 2, 1994, pp. 117–128.

[13]Ashley, H., and Landahl, M., *Aerodynamics of Wings and Bodies*, Dover, New York, 1965, Chap. 2.

[14]Attar, P., Dowell, E., and White, J., "Modeling the LCO of a Delta Wing Using a High Fidelitry Structural Model," AIAA Paper 2004-1692, April 2004.

[15]Katz, J., and Plotkin, A., *Low-Speed Aerodynamics*, 2nd ed., University Press, Cambridge, England, U.K., 2001.

[16]"National Instruments Corporation," Labview, Austin, TX, 1997.